PAPER

Synthesis, magnetic and NMR spectroscopic properties of the MAl₅Pt₃ series (M = Ca, Y, La–Nd, Sm–Er)†

Stefan Engel, [a] Elias C. J. Gießelmann, [a] Lars Schumacher, [b] Yuemei Zhang, [c] Frank Müller[d] and Oliver Janka *[a]

Following recent investigation in the ternary system Sr–Al–Pt led to the discovery of SrAl₅Pt₃ which crystallizes in the orthorhombic YNi₅Si₃ type (*Pnma*) structure. Interestingly, only two more aluminum representatives, CeAl₅Pt₃ and EuAl₅Pt₃, have been reported to adopt this structure type. Therefore, we decided to investigate the existence range of compounds adopting the YNi₅Si₃ type structure. Besides the already known Sr, Ce and Eu members, the series could be extended to Ca, Y and La–Nd as well as Sm–Er. All compounds were synthesized from the elements and characterized by powder X-ray diffraction. While for CaAl₅Pt₃ and LaAl₅Pt₃ also the respective M₂Al₁₆Pt₉ members were observed, the other compounds could be obtained either as X-ray pure materials or with small amounts of Al₃Pt₂ as a side phase. The structure of ErAl₅Pt₃ could be refined from single crystal data, verifying that also the small rare-earth elements adopt the YNi₅Si₃ type structure. Selected members of the series were furthermore characterized by magnetization and susceptibility measurements. Since YAl₅Pt₃ could be obtained as a phase pure material and exhibits no paramagnetic behaviour it was investigated by ²⁷Al MAS NMR investigations. Also, XPS measurements were conducted on this compound to gain an insight into the charge distribution. Finally, quantum-chemical calculations supported the NMR measurements and gave an insight into the chemical bonding and the charge distribution.

1 Introduction

Cerium, europium and ytterbium intermetallics often exhibit interesting physical properties due to their two possible oxidation states. For cerium Ce^{3+} ([Xe] $4f^1$) and Ce^{4+} ([Xe] $4f^0$) are known while europium exhibits Eu^{3+} ([Xe] $4f^6$) and Eu^{2+} ([Xe] $4f^7$) and ytterbium Yb^{3+} ([Xe] $4f^{13}$) and Yb^{2+} ([Xe] $4f^{14}$). Of these, Ce^{4+} and Yb^{2+} are diamagnetic due to their empty and full 4f shell, respectively.[1,2] Eu^{2+} has a half-filled 4f shell ($S = 7/2$, isoelectronic to Gd^{3+}) and therefore exhibits a high magnetic moment of $\mu_{theo} = 7.94\mu_B$. For Eu^{3+} ($S = 3$, $L = 3$) in total seven states of the multiplet ^7F_J exist with the ground state being $^7F_0$. The ground state is diamagnetic due to spin–orbit coupling.

However, the lowest state is only solely considered when the separation of the multiplet components is sufficiently large compared to k_BT. Therefore, the contributions of the different components of the multiplet have to be taken into account for higher temperatures. The paramagnetic susceptibility can be expressed with the help of the Van Vleck theory.[3] The availability of a second oxidation state, however, can result in numerous interesting physical phenomena. Static mixed valence states can be found (Eu_3O_4,[4–6] Eu_3S_4,[7] or $EuPPt$[8]) as well as intermetallic valence fluctuation materials (*e.g.* $CeAl_3$,[9,10] $Yb_4Ga_{24}Pt_9$,[11] $CeMo_2Si_2C$,[12] $CeAlRu_{1-x}Ni_x$,[13] $Ce_2Sn_5Rh_3$,[14] $CeCu_2Si_2$,[15] $EuCu_2Si_2$,[15,16] $YbCu_2Si_2$[15]). A rather rare feature is a temperature or pressure dependent valence phase transition. Well known transitions of this type are *e.g.* the ones from metallic α-Ce to γ-Ce,[17] where electron localization takes place, accompanied by a drastic volume effect. In $EuPPt$,[18] $EuCo_2As_2$ and $YbAl_3$ pressure dependent shifts of the Eu/Yb valence are observed.[19,20] Finally, $CeNi_{1-x}Co_xSn$,[21] and $Yb_{1-x}In_xCu_2$[22–24] exhibit at least partial temperature dependent valence phase transitions. $EuSi_2Pd_2$,[25,26] $EuSi_2(Ir_{1-x}Pd_x)_2$,[27] $EuSi_2(Pd_{1-x}Au_x)_2$,[28] $Eu_2Al_{15}Pt_6$[29] and $YbAl_3Pd_2$[30] all show valence phase transitions in different expressions. Some review articles summarize at least some aspects of intermetallic cerium,[31–36] europium[37] and ytterbium[38] intermetallics.

ᵃInorganic Solid State Chemistry, Saarland University, Campus C4 1, 66123 Saarbrücken, Germany. E-mail: oliver.janka@uni-saarland.de
ᵇInstitut für Anorganische und Analytische Chemie, Universität Münster, Corrensstrasse 28/30, 48149 Münster, Germany
ᶜDepartment of Chemistry and Physics, Warren Wilson College, Swannanoa, NC, 28778, USA
ᵈExperimental Physics and Center for Biophysics, Saarland University, Campus E2 9, 66123 Saarbrücken, Germany
†Electronic supplementary information (ESI) available. CCDC 2349082. For ESI and crystallographic data in CIF or other electronic format see DOI: https://doi.org/10.1039/d4dt01296h

Recently, we reported on a new compound in the ternary system Sr–Al–Pt, $SrAl_5Pt_3$,[39] which adopts the orthorhombic YNi_5Si_3 type structure (*Pnma*).[40] It is furthermore isostructural to $CeAl_5Pt_3$ and $EuAl_5Pt_3$. The europium compound shows antiferromagnetic ordering and an interesting change in electronic states under pressure.[41] Since three compounds are known to crystallize in the same structure type, the question arose if other rare-earth or alkaline-earth members can be synthesized. Here we report that the series could be extended to Ca, Y and La–Nd as well as Sm–Er. All compounds were synthesized from the elements and characterized by powder X-ray diffraction. The structure of $ErAl_5Pt_3$ was refined from single crystal data, YAl_5Pt_3 was investigated by ^{27}Al MAS NMR measurements. Furthermore, XPS measurements were conducted on YAl_5Pt_3 and Al_3Pt_2 and quantum-chemical calculations supported the NMR measurements and gave an insight into the chemical bonding and the charge distribution.

2　Experimental

2.1　Synthesis

All members of the MAl_5Pt_3 series were prepared from the elements using calcium pieces (Onyxmet), rare earth ingots (Onyxmet), platinum (Agosi AG) and aluminum pieces (Onyxmet), all with stated purities above 99.5%. Samples were prepared on a 100 to 150 mg scale. The early rare earth elements were stored under an argon atmosphere in a dry box (MBraun, Garching, Germany). In all cases, the starting materials were arc-melted[42] in a custom build arc-melting apparatus in a water-cooled copper hearth under 800 mbar argon pressure using the ideal ratios of M : Al : Pt (1 : 5 : 3). To achieve homogeneous samples, the arc-melting was repeated three times and the buttons were turned over in between. For calcium and europium, the pieces were wrapped in aluminum foil (Alujet, Mammendorf, Germany). In all cases, no significant evaporation was observed, as determined by weighing the arc-melted beads after the reaction. The argon gas was purified over a titanium sponge (873 K), molecular sieves, activated carbon and silica gel prior to the use. Subsequently, the samples were enclosed in evacuated silica tubes and annealed in muffle furnaces. They were heated to 973 K within two hours and then kept at this temperature for 14 days. Afterwards they were cooled to room temperature with 2 K h^{-1}. All samples are metallic, ground powders (particle size >100 μm) are grey and insensitive to air over months.

2.2　X-ray diffraction

The pulverized samples were investigated at room temperature on a D8-A25-Advance diffractometer (Bruker, Karlsruhe, Germany) in Bragg–Brentano θ–θ-geometry (goniometer radius 280 mm) with Cu K_α-radiation (λ = 154.0596 pm). Diffraction patterns were recorded between 6 and 130° 2θ with a step size of 0.013° and a total scan time of 1 h. A 12 μm Ni foil working as K_β filter and a variable divergence slit were mounted at the primary beam side. A LYNXEYE detector with 192 channels was used at the secondary beam side. The recorded data was evaluated using the Bruker TOPAS 5.0 software,[43] with the observed reflections being treated *via* single-line fits. The refined lattice parameters are given in Table 1. Powder patterns of all samples are depicted in Fig. S1–S12.†

Lath shaped crystal fragments of $ErAl_5Pt_3$ were obtained from the as-cast buttons. The crystals were glued to glass fibers using beeswax. An intensity data set of a suitable crystal was collected at room temperature using a Bruker X8 APEX2 diffractometer (Bruker, Karlsruhe, Germany). A multi-scan absorption correction using SadABS[46] was applied to the data set. All relevant crystallographic data, deposition and details of the data collection and evaluation are listed in Tables 2–4.

CSD 2349082 contains the supplementary crystallographic data for this paper.†

2.3　Scanning electron microscopy

The powdered bulk samples of $NdAl_5Pt_3$, $GdAl_5Pt_3$ and $ErAl_5Pt_3$ were attached to a sticky carbon tape and semiquantitatively analyzed in a JEOL 7000F (Jeol, Freising, Germany) scanning electron microscope (SEM) equipped with an EDAX Genesis 2000 energy-dispersive X-ray spectroscopy (EDX) detector (EDAX, Unterschleissheim, Germany). Results are listed in Table 5.

2.4　Magnetic measurements

Annealed pieces or powder of the respective X-ray pure $REAl_5Pt_3$ (RE = Y, Ce–Nd, Gd–Ho) samples were attached to the sample holder rod of a Vibrating Sample Magnetometer (VSM) using Kapton-foil or PE capsules for measuring the magnetization $M(H,T)$ in a Quantum Design Physical Property

Table 1 Lattice parameters (powder, single crystal and literature data), and unit cell volumes of the members of the MAl_5Pt_3 series as well as selected structurally related compounds

Compound	a (pm)	b (pm)	c (pm)	V (nm^3)	Ref.
$CaAl_5Pt_3$^{SC}	2050.3(1)	409.0(1)	736.4(1)	0.6175	a
$SrAl_5Pt_3$^{L,SC}	2065.04(7)	413.74(1)	738.98(3)	0.6314	39
$SrAl_5Pt_3$^{L,P}	2067.07(6)	414.16(2)	739.88(3)	0.6334	39
YAl_5Pt_3^{P}	2052.8(1)	406.7(1)	728.7(1)	0.6084	a
$LaAl_5Pt_3$^{P}	2068.7(1)	415.5(1)	732.2(1)	0.6293	a
$CeAl_5Pt_3$^{L}	2065.1(4)	413.81(8)	728.42(15)	0.6225	40
$CeAl_5Pt_3$^{P}	2063.9(1)	414.0(1)	730.1(1)	0.6239	a
$PrAl_5Pt_3$^{P}	2061.4(2)	413.0(1)	729.6(1)	0.6212	a
$NdAl_5Pt_3$^{P}	2059.9(1)	412.1(1)	729.3(1)	0.6190	a
$SmAl_5Pt_3$^{P}	2057.0(1)	410.2(1)	728.5(1)	0.6148	a
$EuAl_5Pt_3$^{L}	2066.2(3)	412.58(6)	738.16(11)	0.6293	41
$GdAl_5Pt_3$^{P}	2055.3(2)	408.7(1)	728.3(2)	0.6117	a
$TbAl_5Pt_3$^{P}	2052.9(1)	407.7(1)	728.2(1)	0.6095	a
$DyAl_5Pt_3$^{P}	2051.5(1)	406.7(1)	728.5(1)	0.6079	a
$HoAl_5Pt_3$^{P}	2050.4(1)	405.9(1)	729.1(1)	0.6067	a
$ErAl_5Pt_3$^{P}	2048.4(1)	405.1(1)	729.3(1)	0.6052	a
$ErAl_5Pt_3$^{SC}	2045.82(6)	404.40(1)	728.45(2)	0.6027	a
$CaGa_5Pt_3$^{L}	2082.5(4)	406.05(8)	739.2(1)	0.6251	44
$SrGa_5Pt_3$^{L}	2092.3(1)	413.16(2)	740.88(3)	0.6404	45
$BaGa_5Pt_3$^{L}	2104.8(2)	420.15(4)	747.7(1)	0.6612	44
$BaGa_5Pt_3$^{L}	2104.3(2)	420.11(5)	747.80(8)	0.6611	45
$EuGa_5Pt_3$^{L}	2085.5(5)	412.75(9)	738.7(1)	0.6359	44

^{a} This work; ^{L} literature data; ^{P} powder data; ^{SC} single crystal data.

Paper

Table 2 Crystallographic data and structure refinement for $ErAl_5Pt_3$ (YNi_5Si_3 type, space group $Pnma$, $Z = 4$)

CSD number	2349082
Sum formula	$ErAl_5Pt_3$
Formula weight, g mol^{-1}	887.4
Lattice parameters	see Table 1
Calcd density, g cm^{-3}	9.78
Crystal size, μm^3	120 × 40 × 30
Diffractometer	Bruker X8 APEX2
Wavelength; λ, pm	0.71073
Absorption correction	Multi-scan Bruker SadABS
Abs. coefficient, mm^{-1}	83.8
$F(000)$, e	1468
θ range, °	2.97–33.15
Range hkl	−31, +21; ±6; −10, +11
Total no. reflections	8867
Independent reflections/R_{int}	1279/0.0636
Reflections $I > 3\sigma(I)/R_\sigma$	950/0.0494
Data/parameters	1279/56
Goodness of fit on F^2	1.09
R_1/wR_2 for $I > 3\sigma(I)$	0.0291/0.0594
R_1/wR_2 (all data)	0.0457/0.0650
Extinction coefficient	31(7)
Extinction scheme	Lorentzian isotropic[47]
Larg. diff. peak/hole, e Å^{-3}	+3.64/−2.64

Measurement System (PPMS2) or a Quantum Design PPMS DynaCool system. All samples were investigated in the temperature range of 3–300 K or 1.9–300 K with applied external magnetic fields of up to 80/90 kOe. The results of the magnetic measurements are given in Table 6.

2.5 ^{27}Al solid-state NMR spectroscopy

The ^{27}Al MAS-NMR spectra of YAl_5Pt_3 were recorded at 104.31 MHz on an Avance III 400 WB spectrometer (Bruker, Billerica, US; 9.4 T) using magic-angle spinning (MAS) conditions. The sample was ground to a fine powder and mixed with an appropriate amount of NaCl (sample : NaCl = 1 : 9), to reduce the density and the electrical conductivity of the sample. The diluted sample was loaded into a cylindrical ZrO_2 rotor with a diameter of 4 mm and spun at the magic angle with a frequency of 10/13 kHz. A single-pulse experiment with a typical pulse length of 0.83 μs and a relaxation delay of 1 s

Table 4 Interatomic distances (pm) in of $ErAl_5Pt_3$ (YNi_5Si_3 type, space group $Pnma$). All distances of the first coordination spheres are listed. Standard deviations are equal or smaller than 0.2 pm

Atom	n			Atom	n		
Er	2	Pt3	315.5	Al1	1	Pt1	251.4
	2	Pt1	316.2		1	Pt2	263.4
	2	Pt2	317.2		2	Pt1	264.1
	1	Al5	318.0		2	Al5	274.3
	2	Al2	321.4		2	Al1	278.6
	1	Al3	337.8		1	Al4	306.9
	2	Al1	337.8	Al2	1	Pt3	252.1
	2	Al3	338.2		1	Pt1	258.9
	1	Al4	348.9		2	Pt3	260.0
	1	Al1	352.4		1	Al3	280.4
	1	Al2	357.3		2	Al3	287.1
Pt1	1	Al5	246.9		2	Al4	293.3
	1	Al1	251.4	Al3	1	Pt3	247.2
	1	Al2	258.9		1	Pt2	251.9
	2	Al4	263.6		2	Pt3	255.0
	2	Al1	264.1		1	Al2	280.4
	1	Pt2	308.4		2	Al2	287.1
Pt2	2	Al5	248.4		2	Al4	310.7
	1	Al3	251.9	Al4	1	Pt3	251.3
	1	Al5	252.2		2	Pt1	263.6
	1	Al1	263.4		2	Pt2	269.9
	2	Al4	269.9		1	Al5	284.4
	1	Pt1	308.4		2	Al2	293.3
Pt3	1	Al3	247.2		1	Al1	306.9
	1	Al4	251.3		2	Al3	310.7
	1	Al2	252.1		2	Al5	342.7
	2	Al3	255.0	Al5	1	Pt1	246.9
	2	Al2	260.0		2	Pt2	248.4
					1	Pt2	252.2
					2	Al5	272.1
					2	Al1	274.3
					1	Al4	284.4

Table 5 SEM-EDX data of selected members of the $REAl_5Pt_3$ series. Standard deviations are ±2 at%

Compound	RE (at%)	Al (at%)	Pt (at%)
Ideal composition	11.1	55.6	33.3
$NdAl_5Pt_3$	10	55	35
$GdAl_5Pt_3$	11	53	36
$ErAl_5Pt_3$	11	55	34

Table 3 Atomic coordinates and displacement parameters (in pm^2) of $ErAl_5Pt_3$ (YNi_5Si_3 type, space group $Pnma$, all atoms on Wyckoff positions $4c$: x, 1/4, z)

Atom	x	z	U_{11}	U_{22}	U_{33}	U_{13}	U_{eq} [a]
Er	0.36014(3)	0.87991(8)	81(3)	74(3)	101(3)	7(2)	85(3)
Al1	0.0076(2)	0.3702(5)	57(2)	67(2)	71(3)	−1(2)	65(2)
Al2	0.2011(2)	0.6766(5)	54(2)	60(2)	82(2)	1(2)	65(2)
Al3	0.2081(2)	0.0610(5)	70(2)	50(2)	69(2)	1(2)	63(2)
Al4	0.3809(2)	0.3553(5)	55(17)	54(18)	68(18)	−5(13)	59(18)
Al5	0.4842(2)	0.6168(5)	70(17)	79(19)	47(18)	−6(13)	65(18)
Pt1	0.07482(2)	0.65917(7)	73(17)	36(18)	78(19)	16(14)	62(18)
Pt2	0.08523(2)	0.08160(7)	24(16)	18(16)	76(18)	5(13)	39(17)
Pt3	0.25819(2)	0.36976(7)	57(17)	69(18)	87(19)	−1(14)	71(18)

[a] The isotropic displacement parameter U_{eq} is defined as: $U_{eq} = 1/3 (U_{11} + U_{22} + U_{33})$ (pm^2); $U_{12} = U_{23} = 0$. Standard deviations are given in parentheses.

Table 6 Physical properties of the REAl$_5$Pt$_3$ (RE = Y, Ce–Nd, Gd–Ho) series: T_N, Néel temperature; μ_{eff}, effective magnetic moment; μ_{theo}, theoretical magnetic moment; θ_P, paramagnetic Curie temperature; H_{crit}, critical field for meta-magnetic transition; μ_{sat}, experimental saturation magnetization; $g_J \times J$, theoretical saturation magnetization

Compound	T_N (K)	μ_{eff} (μ_B)	μ_{theo} (μ_B)	θ_P (K)	H_{crit} (kOe)	μ_{sat} (μ_B/RE^{3+})	$g_J \times J$ (μ_B/RE^{3+})
YAl$_5$Pt$_3$	Pauli-paramagnetic, non-superconducting, χ(300 K) = +8.63(1) × 10^{-5} emu mol^{-1}						
CeAl$_5$Pt$_3$	—	2.76(1)	2.54	−41(1)	—	0.99(1)^a	2.14
PrAl$_5$Pt$_3$	—	3.69(1)	3.58	−13(1)	4.4(1)	2.28(1)^b	3.20
NdAl$_5$Pt$_3$	5.1(1)	3.82(1)	3.62	+18(1)	26.7(1)	2.98(1)^a	3.27
GdAl$_5$Pt$_3$	8.7(1)	7.99(1)	7.94	−7(1)	—	2.98(1)^a	7
TbAl$_5$Pt$_3$	15.3(1)	9.49(1)	9.72	+16(1)	33.2(1)	5.36(1)^a	9
DyAl$_5$Pt$_3$	5.8(1)	10.83(1)	10.65	+9(1)	9.8(1)	7.85(1)^b	10
HoAl$_5$Pt$_3$	2.4(1)	10.95(1)	10.61	+19(1)	5.1(1)	8.78(1)^a	10

^{a} 1.8 K, 90 kOe. ^{b} 3 K, 80 kOe.

Table 7 Summary of the NMR observables of YAl$_5$Pt$_3$, extracted from the DMFit simulation of the ^{27}Al MAS-NMR spectra with δ being the resonance (in ppm), C_Q the quadrupolar parameter (in kHz), η_Q the asymmetry parameter and G/L the Gaussian to Lorentz ratio. Theoretically calculated values from DFT are given with the subscript calc

Site	δ	FWHM	$C_{Q,calc}$	$\eta_{Q,theo}$
Signal 1	693	31	—	—
Signal 2	642	24	—	—
Signal 3	602	13	—	—
Signal 4	567	17	—	—
Signal 5	510	14	—	—
Al1 (4c)	—	—	−2484	0.771
Al2 (4c)	—	—	−1642	0.523
Al3 (4c)	—	—	−2302	0.425
Al4 (4c)	—	—	+3819	0.519
Al5 (4c)	—	—	+5487	0.690

was conducted. Resonance shifts were referenced to aqueous 1 molar AlCl$_3$ solutions. The NMR-spectra were recorded using the Bruker TOPSPIN software,[48] the analysis was performed with the help of the DMFIT program package.[49] The extracted data is compiled in Table 7.

2.6 X-ray photoelectron spectroscopy (XPS)

For XPS experiments an ESCALab Mk II spectrometer by *Vacuum Generators* with non-monochromatic Al-K$_\alpha$ radiation ($\hbar\omega$ = 1486.6 eV) was used. The original 150°-type hemispherical analyzer with a three channeltron detector system was replaced by a 180°-type *PreVac* EA 15 analyzer with a multichannelplate detector. All spectra were recorded in normal emission mode (polar angle ϑ = 0°) at a pass energy of 50 eV for survey spectra and 20 eV for detail spectra. The step widths in binding energy were 1.0 eV for survey spectra and 100 meV for detail spectra.

Powders of Al$_3$Pt$_2$ and YAl$_5$Pt$_3$ were pressed to pellets (diameter approx. 4 mm) and glued by a conductive carbon tape

on an Al sample holder (diameter slightly lower than 4 mm to avoid spectral features from the sample holder and the tape). Due to the strong charging of the Al$_3$Pt$_2$ and YAl$_5$Pt$_3$ samples the C 1s peak was used for calibration of the binding energy E_B, *i.e.* all spectra were shifted in binding energy by $\Delta = E_B$(C 1s) − E_B(C 1s$_{HOPG}$) with E_B(C 1s$_{HOPG}$) = 284.3 eV as probed on an *in situ* cleaved HOPG sample (Highly Oriented Pyrolytic Graphite). Pt 4f and Al 2s reference spectra were recorded on a sample from a Pt foil (cleaned by Ar ion etching) and an Al sheet (with the oxide only partially removed by Ar ion etching), respectively.

2.7 Quantum-chemical calculations

Density functional theory (DFT) calculations of YAl$_5$Pt$_3$ were performed using the projector augmented wave method (PAW) of Blöchl[50,51] coded in the Vienna *ab initio* simulation package (VASP).[52,53] All VASP calculations employed the generalized gradient approximation (GGA) with exchange and correlation treated by Perdew-Burke-Enzerhof (PBE).[54] The cut-off energy for the plane wave calculations was set to 500 eV and the Brillouin zone integration was carried out using 3 × 15 × 9 k-point meshes. NMR parameters were evaluated through the field gradient tensor calculations in VASP with the nuclear quadrupole moment of 146.6 mb for ^{27}Al. The Bader charge analysis was based on VASP calculations with subsequent calculations using the Bader program developed by the Henkelman group.[55–57] Results of the Bader charge calculations are listed in Table 8. Chemical bonding was assessed *via* crystal orbital Hamiltonian population (COHP) analysis using the Stuttgart version of the tight-binding, linear muffin-tin orbital (TB-LMTO) method with the atomic spheres approximation.[58] Within TB-LMTO, exchange and correlation were treated using the von Barth-Hedin local density approximation (LDA). All relativistic effects except for spin–orbit coupling were taken into account using a scalar relativistic

Table 8 Bader charges in YAl$_5$Pt$_3$ from non-spin-polarized DFT calculations

YAl$_5$Pt$_3$	Y	Al1	Al2	Al3	Al4	Al5	Pt1	Pt2	Pt3
Charge	+1.25	+0.76	+0.79	+0.91	+0.93	+0.93	−1.80	−1.80	−1.98

approximation.[59] The basis sets were 5s/(5p)/4d/(4f) for Y, 6s/6p/5d/(5f) for Pt, and 3s/3p/(3d) for Al, with orbitals in parentheses down-folded.[60] The Brillouin zone was sampled by 280 k-points. Results of bonding analysis are summarized in Table 9.

3 Results

3.1 Powder X-ray diffraction

All samples were prepared with the nominal composition of MAl_5Pt_3 (M = Ca, Y, La–Nd, Sm–Er) in analogy to $SrAl_5Pt_3$,[39] $EuAl_5Pt_3$,[41] and $CeAl_5Pt_3$.[40] The powder X-ray diffraction patterns clearly indicate the formation of the title compounds as well as them being isostructural to their Sr/Eu/Ce analogues. Most of the compounds could be obtained as X-ray pure

Table 9 Atomic interactions/distances and their corresponding integrated COHPs (ICOHPs) in eV per bond and eV per f.u. of YAl_5Pt_3 (YNi_5Si_3 type, space group $Pnma$, $Z = 4$). All interactions/distances of the first coordination spheres are listed

Interaction	Counts	Distance	ICOHP/bond	ICOHP/f.u.
Y–Pt1	2	318.1	−0.65	−1.30
Y–Pt2	2	319.2	−0.65	−1.30
Y–Pt3	2	318.2	−0.62	−1.23
Y–Al1	2	339.3	−0.40	−0.81
	1	353.3	−0.30	−0.30
Y–Al2	2	322.5	−0.51	−1.02
	1	358.5	−0.29	−0.29
Y–Al3	2	336.4	−0.48	−0.95
	1	339.8	−0.37	−0.37
Y–Al4	1	347.6	−0.36	−0.36
Y–Al5	1	319.0	−0.46	−0.46
Sum				**−8.40 (14.3%)**
Pt1–Al1	1	251.9	−2.19	−2.19
	2	264.8	−1.74	−3.48
Pt1–Al2	1	259.3	−1.96	−1.96
Pt1–Al4	2	263.7	−1.91	−3.81
Pt1–Al5	1	246.2	−2.25	−2.25
Pt2–Al1	1	264.0	−1.80	−1.80
Pt2–Al3	1	252.5	−2.36	−2.36
Pt2–Al4	2	270.8	−1.73	−3.47
Pt2–Al5	2	249.1	−2.17	−4.35
	1	252.1	−2.05	−2.05
Pt3–Al2	1	252.9	−2.07	−2.07
	2	261.2	−1.81	−3.63
Pt3–Al3	1	247.7	−2.21	−2.21
	2	255.8	−1.98	−3.97
Pt3–Al4	1	250.2	−2.32	−2.32
Sum				**−39.6 (67.4%)**
Pt1–Pt2	1	306.5	−0.65	−0.65
Sum				**−0.65 (1.10%)**
Al1–Al1	2	279.5	−1.09	−2.19
Al1–Al4	1	306.8	−0.63	−0.63
Al1–Al5	2	275.2	−1.14	−2.29
Al2–Al3	1	282.4	−0.84	−0.84
	2	288.7	−0.84	−1.68
Al2–Al4	2	292.5	−0.80	−1.61
Al3–Al4	2	314.0	−0.41	−0.82
Al4–Al5	2	284.8	−0.98	−1.95
	1	344.0	−0.07	−0.07
Al5–Al5	2	272.9	−0.11	−0.22
Sum				**−10.1 (17.2%)**
Overall ICOHP				**−58.8**

materials crystallizing in the orthorhombic YNi_5Si_3 type structure ($Pnma$).[61] But especially for lanthanum and calcium, orthorhombic $M_2Al_{16}Pt_9$ ($Immm$, $Ce_2Al_{16}Pt_9$ type)[62] could be identified as a side phase. In some cases, also trigonal Al_3Pt_2 ($P\bar{3}m1$, Al_3Ni_2 type)[63,64] was observed as binary by-product. In many cases, annealing led to X-ray pure samples or a drastic reduction of the Al_3Pt_2 amounts to <2 mass%. Fig. 1 depicts the trend of the unit cell volumes plotted *versus* the ionic radius of the respective metal ions. Most of the rare earth cations exhibit a trivalent oxidation state, however, europium and the alkaline earth metals are divalent in these compounds as can be seen from the significantly larger unit cell volumes. Also, the isostructural MGa_5Pt_3 (M = Ca, Sr, Eu, Ba)[44,45] exhibit slightly larger unit cells as shown in Table 1 and Fig. 1.

3.2 Single crystal X-ray diffraction and structure refinement

Analysis of the obtained single crystal X-ray diffraction data of $ErAl_5Pt_3$ revealed an orthorhombic lattice and space group $Pnma$ was found to be correct. The structure was solved using the charge flipping algorithm of Superflip[65] and a least squares refinement on F^2 using the program Jana2006[66,67] was carried out. All atomic positions were refined with anisotropic displacement parameters and as a check for correct compositions, the occupancy parameters were refined in a separate series of least-square refinements. All sites were fully occupied within three standard deviations leading to the targeted compositions. Final difference Fourier syntheses were contour less. From the Pearson database,[68] isotypism with $CeAl_5Pt_3$[40] adopting the YNi_5Si_3 type[61] was deduced. In contrast to UFe_5As_3 and related compounds no twinning was observed.[69] Details of the structure determination, atomic parameters and interatomic distances can be found in Tables 2–4. When looking at the refined anisotropic displacement parameters (ADP) of the atoms, Er exhibits a value of 85 pm^2, which is larger than the

Fig. 1 Plot of the unit cell volumes (in nm^3) for the MAl_5Pt_3 series (M = Ca, Sr, Y, La–Nd, Sm–Er) *versus* the M^{n+} radius (in pm). Formally divalent metal atoms are depicted in green, trivalent ones in black, the members of the gallium series are shown in orange.

one of Pt and Al. This might be explained by the fact that $ErAl_5Pt_3$ is the last compound of this series, leading to the assumption that the Er atoms rattle inside the cavities of the polyanionic framework, leading to an increased ADP.

CSD 2349082 contains the supplementary crystallographic data for this paper.†

3.3 Crystal chemistry

All members of the MAl_5Pt_3 series crystallizes in the orthorhombic crystal system with space group *Pnma* (*oP*36, c^9) and are isostructural with the aluminum representatives $CeAl_5Pt_3$, $EuAl_5Pt_3$ and $SrAl_5Pt_3$.[39–41] Besides the aluminum compounds also several gallium compounds MGa_5Pt_3 (M = Ca–Ba, Eu)[44,45] have been reported, having the corresponding composition. These compounds, however, should not be considered isostructural to the prototypic YNi_5Si_3 structure,[61] but rather isopointal. Especially since the $[Ni_5Si_3]^{\delta-}$ polyanion exhibits a different transition metal to main group element ratio, compared to the respective platinides of aluminum and gallium.

Fig. 2a exemplarily depicts the crystal structure of YAl_5Pt_3 as projection along [010]. The Y atoms exhibit a slightly distorted hexagonal prismatic coordination environment with an alternating arrangement of the Al and Pt atoms within the hexagon, but a congruent arrangement of top and bottom face is observed (Fig. 3). The $Y@Al_6Pt_6$ form strands along [010] *via* condensation of their hexagonal faces. Within the prism, the interatomic Y–Al distances range between 322 and 342 pm, while the Y–Pt distances are between 328 and 330 pm. Both, the Y–Al and Y–Pt distances are in line with the ones found in binary intermetallics *e.g.* YAl_2 (MgCu$_2$ type, 325–340 pm [70]), YAl_3 (Mg$_3$Cd type, 302–310 pm [71]), YPt_2 (MgCu$_2$ type, 314–328 pm [70]) or YPt_3 (Cu$_3$Au type, 288 pm [72]) as well as with the sum of the covalent radii (Y + Al = 162 + 125 =
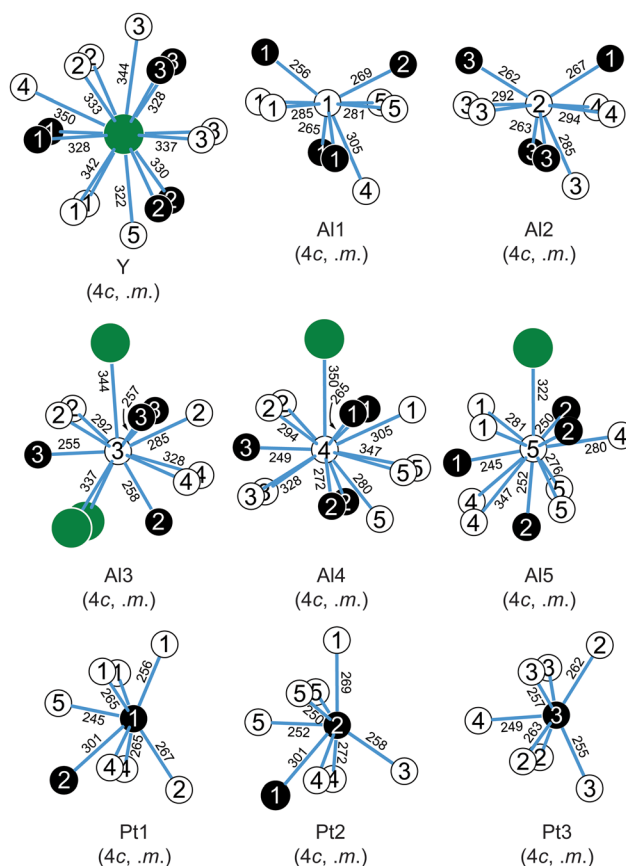

Fig. 3 Coordination environments surrounding the Y, Pt and Al atoms in the structure of YAl_5Pt_3. Sr, Pt and Al atoms are shown as green, white and black circles, respectively. Wyckoff sites, site symmetries and interatomic distances (in pm) are given.
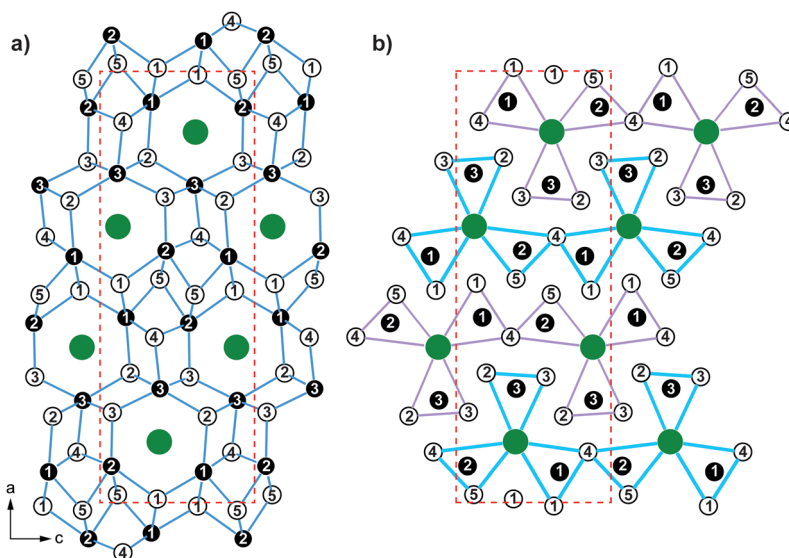

Fig. 2 Unit cell of YAl_5Pt_3 as projection along [010] (a) highlighting the polyanionic $[Al_5Pt_3]^{\delta-}$ framework (the shortest Al−Pt interactions are emphasized in blue) and (b) using $X@M_2T_4$ prisms to illustrate the structure (the interactions forming the prisms are highlighted in blue and purple). Y, Al and Pt atoms are shown in green, white and black circles, respectively.

287 pm; Y + Pt = 162 + 129 = 291 pm [73]). Similar distances can be observed in ternary compounds of the Y–Al–Pt system like YAlPt (TiNiSi type, Y–Al: 308–336 pm; Y–Pt: 257–267 pm),[74] YAl_2Pt ($MgAl_2Cu$ type, Y–Al: 287–305 pm; Y–Pt: 287–308 pm),[75] $Y_4Al_{24}Pt_9$ (own type, Y–Al: 304–321 pm; Y–Pt: 328–336 pm),[76] YAl_3Pt_2 (own type, Y–Al: 329–348 pm; Y–Pt: 301–316 pm),[77] YAl_2Pt_5 ($ZrAl_5Ni_2$ type, Y–Al: no contacts; Y–Pt: 288–302 pm),[78] Y_4AlPt (Gd_4InRh type, Y–Al: 324–348 pm; Y–Pt: 281–347 pm)[79] or $Y_{10}Al_3Pt$ ($Y_{10}Cd_3Ru$ type, Y–Al: 324–348 pm; Y–Pt: 275 & 349 pm).[80]

The $[Al_5Pt_3]^{\delta-}$ polyanion is formed by five crystallographically independent aluminum and three platinum sites (Fig. 2). All Pt sites exhibit a coordination number of seven with a highly asymmetrical coordination environment and interatomic Al–Pt distances between 247 and 270 pm. These agree well with those in binary (AlPt: 248–273 pm;[81,82] Al_2Pt: 256 pm;[83] Al_3Pt_2: 255–286 pm [63,64]) and ternary intermetallics (YAlPt: Al–Pt 308–336 pm,[74] YAl_2Pt: Al–Pt 287–305 pm,[75] YAl_3Pt_2: Al–Pt 329–348 pm [77]) as well as with the sum of the covalent radii (Pt + Al = 129 + 125 = 254 pm [73]). The respective homoatomic distances (YAl_5Pt_3: Pt–Pt: 306 pm; Al–Al: 273–293 pm) agree with what is observed in elemental Al (286 pm [84]), therefore suggesting partial bonding contributions while the Pt–Pt distances are significantly longer compared to the distances found in the elemental Pt (277 pm [85]) or the sum of the covalent radii (Al: 250 pm; Pt: 258 pm).[73] Another possibility to describe the YNi_5Si_3 type structure, especially when compared to other structure types of the same stoichiometry MT_5X_3 such as the UFe_5As_3, the $LaCo_5P_3$, the UCo_5Si_3 or the YCo_5P_3 type structures, is to use trigonal prisms surrounding the As, P or Si atoms. These $X@M_2T_4$ prisms condense *via* common M_2 or T_2 edges to form "shamrock" like structures that are further condensed. One possibility is to form chains are linear in the case of the YNi_5Si_3 type structure (Fig. 2b). A more detailed description can be found in a recent publication.[69]

3.4 Scanning electron microscopy

Powders of $NdAl_5Pt_3$, $GdAl_5Pt_3$ and $ErAl_5Pt_3$ were investigated by SEM-EDX. The average of three point measurements are given in Table 5 and are in good agreement with the ideal composition (11.1 at% M, 55.6 at% Al, 33.3 at% Pt). The slight deviations can be explained by the irregular sample surface and the not perfect perpendicular orientation of the powder towards the beam. No impurity elements heavier than sodium (detection limit of the instrument) were detected.

3.5 Magnetic measurements

YAl_5Pt_3 is, as expected, a Pauli-paramagnetic material with a positive susceptibility since the Pauli contribution originating from the conduction electrons overcompensates the intrinsic diamagnetism. No superconductivity was observed at 20 Oe down to 2.5 K.

All other X-ray pure members of the $REAl_5Pt_3$ series (RE = Y, Ce–Nd, Gd–Ho) exhibit an open-shell 4f electron configuration leading to paramagnetic behavior. Their effective magnetic
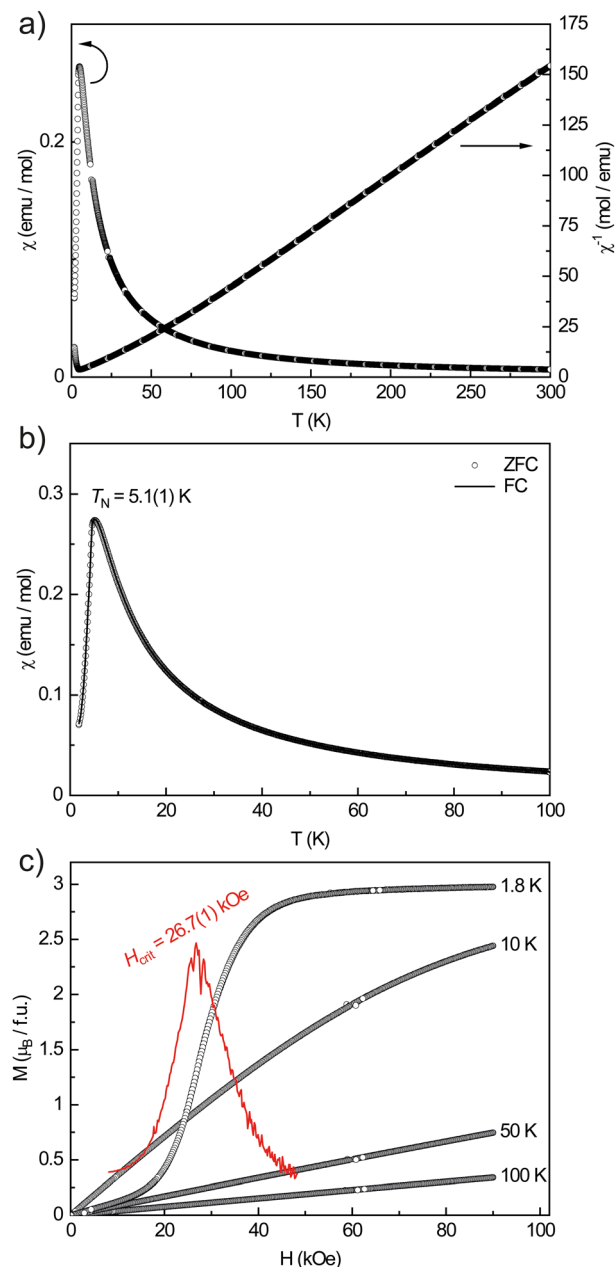

Fig. 4 Magnetic data of $NdAl_5Pt_3$. (a) Temperature dependence of the magnetic and inverse magnetic susceptibility (χ and χ^{-1} data) measured with an applied external field of 10 kOe; (b) zero-field-cooled/field-cooled (ZFC/FC) measurements measured with an applied external field of 100 Oe; (c) magnetization isotherms recorded at 1.8, 10, 50 and 100 K, the inflection point is determined by the first derivative of dM/dH, shown in red.

moments calculated from modified Curie–Weiss fits indicate a stable trivalent oxidation state in all cases in good agreement with the expected moments for the free RE^{3+} cations (Table 6). Fig. 4 exemplarily depicts the magnetic behavior of $NdAl_5Pt_3$. The magnetic susceptibility data recorded between 1.8 and 300 K in zero-field-cooled mode (ZFC) at 10 kOe already shows a maximum at low temperatures indicating an antiferro-

magnetic transition (Fig. 4a). From the inverse susceptibility, the experimental magnetic moment was calculated to be μ_{exp} = 3.82(1)μ_B, in line with Nd^{3+} (μ_{eff} = 3.62μ_B). The positive Weiss constant of θ_P = 18(1) K points towards ferromagnetic interactions in the paramagnetic temperature regime and could be a sign of so called A-type antiferromagnetism in which each layer orders ferromagnetically but antiparallel to adjacent layers.[86] The low field data (100 Oe) was recorded in zero-field-cooled and field-cooled (ZFC/FC) mode between 1.8 and 100 K (Fig. 4b). At T_N = 5.1(1) K a clear maximum can be observed, originating from the antiferromagnetic ordering which causes the magnetic susceptibility to drop below the Néel temperature. Since the ZFC and FC curves are on top of each other, ferromagnetic impurities can be excluded. The magnetization isotherms are finally shown in Fig. 4c. The isotherms recorded at 50 and 100 K are linear up to 90 kOe, indicating Curie paramagnetism at these temperatures. The 10 K isotherm is slightly curved due to the proximity of the magnetic phase transition. The 1.8 K isotherm finally shows a pronounced S-shape indicating a meta-magnetic step. While at low magnetic fields the antiparallel orientation of the spins persists, a spontaneous reorientation is observed at a critical field of H_{crit} = 26.7(1) kOe. The infliction point is determined by the first derivative dM/dH. The saturation magnetization at 1.8 K and 90 kOe reaches μ_{sat} = 2.98(1)μ_B which is close to the theoretical saturation magnetization according to $g_J \times J$ of 3.27μ_B and in line with the almost horizontal trace.

Since the interatomic M–M distances in the whole MAl$_5$Pt$_3$ series are rather large (>550 pm), RKKY (Ruderman-Kittel-Kasuya-Yosida) interactions between the rare-earth atoms are expected. In this case, the magnetic ordering temperatures, in this case the Néel temperatures, should scale with the de Gennes factor G [$(g_J - 1)^2 J(J + 1)$]. Fig. 5 shows the obtained correlation between T_N and G, clearly indicating a deviation from the expected behavior. This points towards crystal field
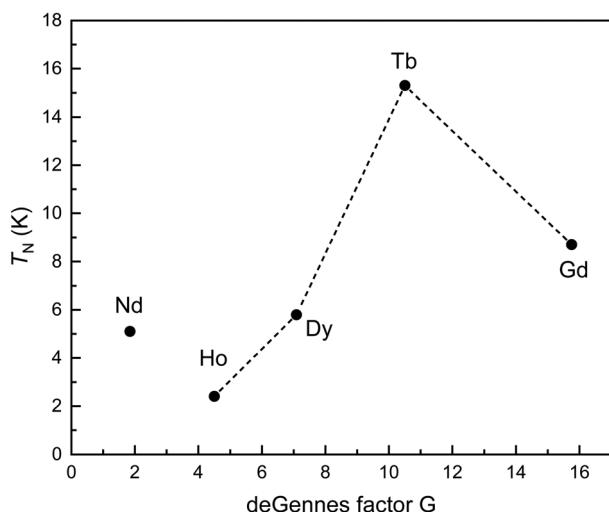
influences in the REAl$_5$Pt$_3$ series. Similar results have been observed for example in the RE$_2$InT$_2$ (RE = La–Nd, Sm, Gd–Lu; T = Ni, Cu, Pd) series.[87–89]

Finally, for some of the other samples, the determined saturation magnetizations (Table 6) are significantly different to the values according to $g_J \times J$ which can either be explained by crystal field effects (see de Gennes scaling) or the polycrystalline nature of the samples.

3.6 ^{27}Al solid-state NMR spectroscopy

Solid-state MAS NMR spectroscopy is a powerful tool to support crystallography. Besides a plain confirmation of the crystal structure (number of sites equals number of signals) also structural distortions or the presence of solid solutions can be probed based on the shape of the e.g. ^{27}Al NMR signal.[78,90–93]

Fig. 6 depicts the results of the ^{27}Al MAS-NMR spectroscopic investigations on YAl$_5$Pt$_3$. Consistent with its crystal structure, the spectrum confirms the presence of five crystallographically independent Al sites. However, only the intense central line originating from the $|+1/2\rangle \leftrightarrow |-1/2\rangle$ transitions of the five Al sites can be modelled with a Gauss-Lorentz fit. Since no significant broadening is observed, one can conclude that the electric quadrupolar couplings C_Q are rather small (in a range <5 MHz) and second order quadrupole effects (SOQE) are not dominant, in line with the results from the quantum-chemical calculations (Table 7). The resonances of these five signals are significantly shifted compared to the standard of an aqueous solution of Al^{3+} (AlCl$_3$), however, they are in line with the reported shifts for intermetallic aluminum compounds. The drastic shift, typically in the range of 200–1200 ppm,[90] is caused by the s-electron spin density at the Fermi level as probed by the ^{27}Al nuclei and dominated by the Knight shift contribution.[90] Under magic angle spinning (MAS) conditions one can potentially observes a wide spinning sideband pattern originating from the outer satellite transitions, $|\pm1/2\rangle \leftrightarrow |\pm3/2\rangle$ and $|\pm3/2\rangle \leftrightarrow |\pm5/2\rangle$, however, this is not the case here.
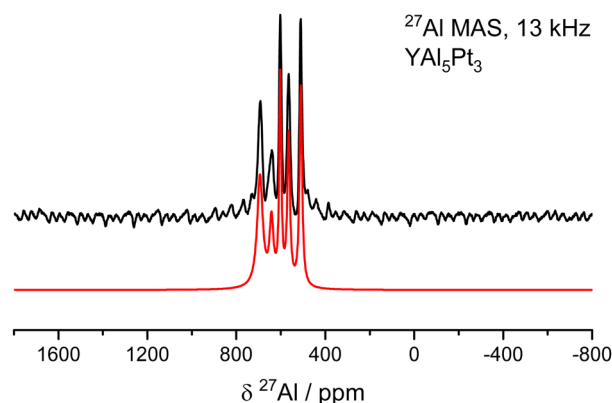

Fig. 5 Plots of the ordering temperatures versus the de Gennes factor $(g_J - 1)^2 J(J + 1)$ for the REAl$_5$Pt$_3$ series.

Fig. 6 ^{27}Al MAS-NMR spectra (black) of YAl$_5$Pt$_3$ (YNi$_5$Si$_3$ type) along with the fit of the central transitions (red).

3.7 XPS

X-ray photoelectron spectra have been recorded to investigate the electronic properties in the synthesized compounds from an experimental point of view. The 4f core levels of, *e.g.*, Pt are very sensitive towards the electronic structure at the respective atom, allowing a spectroscopic approach to analyze the charge transfer in these intermetallic compounds. For intermetallic alkaline earth or rare-earth aluminum compounds with late transition metals, especially with 5d elements, an electron transfer from the AE/RE and Al atoms to the platinum atoms can be observed. This has been shown for quite some instances, *e.g.*, $Ba_3Al_4Pt_4$[94] and the $REAl_3Pt_2$ (RE = Y, Dy–Tm) series.[77] Since the most electronegative elements acquire additional electron density, shifts of the binding energies of the Pt 4f lines towards lower binding energies can be observed in the respective XPS measurements.[94–97] In general, the Pt 4f states can be chosen as a reference as they are intense and sharp enabling the detection of already small shifts. However, it has to be mentioned that the Pt 4f and Al 2p levels have almost the same binding energy.[98]

Fig. 7a depicts the XPS spectra of the Pt 4f lines of elemental Pt (black), YAl_5Pt_3 (red) and Al_3Pt_2 (blue). For the Pt reference (Pt foil) a binding energy of BE(Pt) = 71.0(1) eV was observed, in line with the literature.[98] For YAl_5Pt_3 and Al_3Pt_2 shifts of +0.23 and +0.76 eV were obtained (BE(YAl_5Pt_3) = 71.23 eV; BE(Al_3Pt_2) = 71.76 eV). In contrast to what is intuitionally expected and described before, the shift of the Pt lines to higher binding energies indicates a formal formation of cationic Pt species in both compounds. Given the drastic electronegativity differences (χ(Pt) = 2.28 and χ(Al) = 1.61[73]), a shift towards lower binding energies, in line with an anionic character, is expected. However, a recent HAXPES study has shown, that, although a charge transfer towards an anionic Pt species is expected based on quantum-chemical data, shifts towards formal cationic Pt are visible in binary aluminum platinides.[99] The authors could show, that the QTAIM charges on the Pt atoms correlate with the positive shifts of the Pt 4f binding energies. This was attributed to changes in the Pt 5d orbital occupancies preventing an easy interpretation only based on the shifts of the Pt 4f binding energies in this binary system. Therefore the question arises if this is also applicable in the system reported here.

When looking at the intensities of the $4f_{7/2}$ and $4f_{5/2}$ peaks, however, only the elemental Pt reference shows the expected 4 : 3 ratio.[98] For YAl_5Pt_3 and Al_3Pt_2, the $4f_{5/2}$ peaks seem to be equally high if not higher compared to the $4f_{7/2}$ peak. This is probably either due to at least a second set of Pt 4f levels. For Al, a shift towards higher binding energies, corresponding to a cationic character, is expected. Fig. 7b shows the XPS spectra of the Al 2s lines of elemental Al (black), YAl_5Pt_3 (red) and Al_3Pt_2 (blue). Here, the expected shift can be observed, however, the main peak corresponds to the one of trivalent Al as in Al_2O_3. Subsequently, XPS spectra of the oxygen 1s lines were conducted (Fig. 7c). Here, a signal corresponding to the expected value of Al_2O_3 can be observed for Al_3Pt_2, for YAl_5Pt_3,
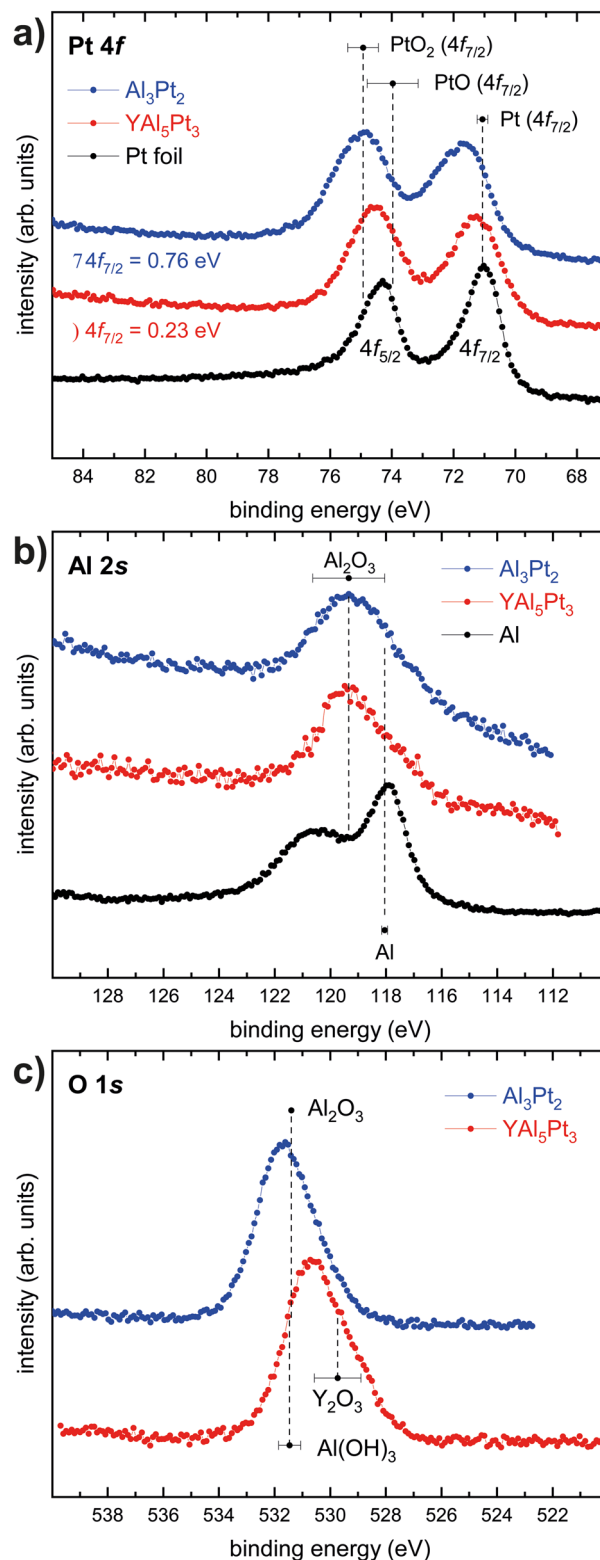

Fig. 7 (a) Pt 4f spectra of YAl_5Pt_3 (red) and Al_3Pt_2 (blue) and Pt (black); (b) Al 2s spectra of YAl_5Pt_3 (red) and Al_3Pt_2 (blue) and Al (black); (a) O 1s spectra of YAl_5Pt_3 (red) and Al_3Pt_2 (blue). Mean values of binding energies and standard deviations are obtained by averaging over all entries in the NIST XPS database for the compounds specified in (a)–(c).[101]

two overlapping lines can be observed that originate from Al_2O_3 and Y_2O_3. This suggests that the surface of the powder particles used for the XPS investigations is oxidized. This leads to the conclusion, that although these XPS investigations show an effect similar to what has been observed and reported for the binary Al–Pt system in literature, here a fully oxidized surface is present. Therefore, the shifts to higher binding energies in line with the literature are probably a mere coincidence. In the investigated samples, Pt atoms in an Al_2O_3 matrix rather than in the intermetallic compounds YAl_5Pt_3 and Al_3Pt_2 were probed in the XPS-accessible subsurface range. Studies on Al containing metallic glasses have shown a similar effect. Here, Al was oxidized throughout the material while all other metals were only oxidized within the first 5 nm below the surface.[100]

3.8 Quantum-chemical calculations

The chemical bonding within YAl_5Pt_3 was investigated through crystal orbital Hamiltonian population (COHP) analysis. The integrated COHP (ICOHP) values, as listed in Table 9, highlights the predominant role of Al–Pt bonds, contributing over 65% to the total ICOHP value. Following these, the interactions of Al–Al are notable, while those involving Y–Al, Y–Pt, and Pt–Pt are relatively weaker. Particularly, the differences in the strengths between Al–Pt (-1.73 to -2.36 eV) and Al–Al interactions (-0.07 to -1.14 eV), in contrast to the Y–Pt (-0.62 to -0.65 eV) and Y–Al (-0.29 to -0.51 eV) ones, suggest the presence of a polyanionic $[Al_5Pt_3]^{\delta-}$ network, with $Y^{\delta+}$ cations occupying the resulting cavities.

The electronic structure of YAl_5Pt_3 was analyzed using density functional theory (DFT) calculations. The electron density of states (DOS) curves for YAl_5Pt_3 are depicted in Fig. 8. Notably, there exists a significant density of states at the Fermi level, indicative of metallic behavior, consistent with the observed silver to grey metallic appearance. The calculated Bader effective charges for YAl_5Pt_3 are detailed in Table 8. Each of the five crystallographically independent Al atoms exhibits positive charges. Moreover, the deviation of all Al atom charges from +3 (with values from +0.76 to +0.93) suggests that the Al–Pt interactions possess a predominantly

covalent character than ionic. This observation aligns with the large negative Al–Pt ICOHP values and supporting the presence of a polyanionic $[Al_5Pt_3]^{\delta-}$ network. Conversely, all Pt atoms demonstrate negative charges. Yttrium (Y) is observed to possess a positive charge of +1.25, which is notably less than a trivalent oxidation state. This suggests significant electron delocalization and robust Y–Pt and Y–Al covalent/metallic interactions, consistent with the noteworthy negative ICOHP values. These findings support the metallic character of YAl_5Pt_3.

4 Conclusion

The MAl_5Pt_3 series with M = Sr, Ce, Eu could be significantly extended to M = Ca, Y and La–Nd as well as Sm–Er. All compounds were synthesized from the elements using arc-melting and subsequent annealing and were characterized by powder X-ray diffraction. For $CaAl_5Pt_3$ and $LaAl_5Pt_3$ also the respective $M_2Al_{16}Pt_9$ members were observed, however, the other compounds could be obtained either as X-ray pure materials or with small amounts of Al_3Pt_2 as side phase. Single-crystal X-ray diffraction studies on $ErAl_5Pt_3$ verified that also the small rare-earth elements adopt the YNi_5Si_3 type structure. For selected members of the series (M = Y, Ce–Nd, Gd–Ho) magnetization and susceptibility measurements were conducted. YAl_5Pt_3 is Pauli-paramagnetic while all other compounds are Curie paramagnets with the RE atoms in the trivalent oxidation state. For M = Nd, Gd–Ho, antiferromagnetic ordering was observed. Since YAl_5Pt_3 was obtained as phase pure material ^{27}Al MAS NMR investigations were conducted. Five signals were observed, in line with the five crystallographic Al positions in the structure. Also, XPS measurements were conducted on this compound to gain an insight into the charge distribution. However, XPS cannot come up with this task due to the oxidation of the surface and the subsurface bulk. Finally, quantum-chemical calculations supported the NMR measurements and gave an insight into the chemical bonding and the expected charge distribution with the Pt atoms being the formal anions while the Y and Al atoms are cationic in nature.
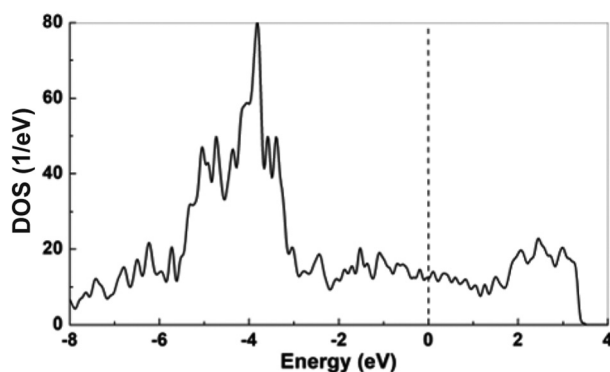
Author contributions

All authors have accepted responsibility for the entire content of this submitted manuscript and approved the submission.

Data availability

The data supporting this article have been included as part of the ESI.† Crystallographic data for $ErAl_5Pt_3$ has been deposited at The Cambridge Crystallographic Data Centre (CCDC) under 2349082.†

Fig. 8 Total density of states of YAl_5Pt_3 from non-spin-polarized DFT calculation, dotted line indicates the Fermi level.

Conflicts of interest

The authors declare no conflicts of interest regarding this article.

Acknowledgements

References

1 J. Jensen and A. R. Mackintosh, *Rare earth magnetism: Structures and excitations*, Clarendon Press, Oxford, 1991.

2 H. Lueken, *Magnetochemie*, B. G. Teubner, Stuttgart, Leipzig, 1999.

3 J. H. van Vleck, *The Theory Of Electric And Magnetic Susceptibilities*, Oxford At The Clarendon Press, 1932.

4 H. Bärnighausen and G. Brauer, *Acta Crystallogr.*, 1962, **15**, 1059.

5 R. Rau, *Acta Crystallogr.*, 1966, **20**, 716–723.

6 F. F. Y. Wang, *Phys. Status Solidi*, 1966, **14**, 189–192.

7 F. L. Carter, *J. Solid State Chem.*, 1972, **5**, 300–313.

8 N. Lossau, H. Kierspel, J. Langen, W. Schlabitz, D. Wohlleben, A. Mewis and C. Sauer, *Z. Phys. B: Condens. Matter*, 1989, **74**, 227–232.

9 K. H. J. Buschow and H. J. Vandall, *Solid State Commun.*, 1970, **8**, 363–365.

10 K. H. Mader and W. M. Swift, *J. Phys. Chem. Solids*, 1968, **29**, 1759–1764.

11 O. Sichevych, Y. Prots, Y. Utsumi, L. Akselrud, M. Schmidt, U. Burkhardt, M. Coduri, W. Schnelle, M. Bobnar, Y.-T. Wang, Y.-H. Wu, K.-D. Tsuei, L. H. Tjeng and Y. Grin, *Inorg. Chem.*, 2017, **56**, 9343–9352.

12 U. B. Paramanik, Anupam, U. Burkhardt, R. Prasad, C. Geibel and Z. Hossain, *J. Alloys Compd.*, 2013, **580**, 435–441.

13 O. Niehaus, U. C. Rodewald, P. M. Abdala, R. S. Touzani, B. P. T. Fokwa and O. Janka, *Inorg. Chem.*, 2014, **53**, 2471–2480.

14 M. B. Gamża, R. Gumeniuk, U. Burkhardt, W. Schnelle, H. Rosner, A. Leithe-Jasper and A. Ślebarski, *Phys. Rev. B*, 2017, **95**, 165142.

15 B. C. Sales and R. Viswanathan, *J. Low Temp. Phys.*, 1976, **23**, 449–467.

16 E. R. Bauminger, D. Froindlich, I. Nowik, S. Ofer, I. Felner and I. Mayer, *Phys. Rev. Lett.*, 1973, **30**, 1053–1056.

17 D. C. Koskenmaki and K. A. Gschneidner, *Handbook on the Physics and Chemistry of Rare Earths*, 1978, vol. 1, pp. 337–377.

18 M. Akihiro, M. Shigeki, U. Masafumi, W. Hirofumi, M. Kazuyuki, U. Yoshiya, M. Masaichiro, K. Naomi, N. Kiyofumi, H. Naohisa, O. Yasuo and I. Naoki, *J. Phys.: Condens. Matter*, 2018, **30**, 105603.

19 R. S. Kumar, A. Svane, G. Vaitheeswaran, V. Kanchana, E. D. Bauer, M. Hu, M. F. Nicol and A. L. Cornelius, *Phys. Rev. B: Condens. Matter Mater. Phys.*, 2008, **78**, 075117.

20 X. Tan, G. Fabbris, D. Haskel, A. A. Yaroslavtsev, H. Cao, C. M. Thompson, K. Kovnir, A. P. Menushenkov, R. V. Chernikov, V. O. Garlea and M. Shatruk, *J. Am. Chem. Soc.*, 2016, **138**, 2724–2731.

21 D. T. Adroja, B. D. Rainford, J. M. de Teresa, A. del Moral, M. R. Ibarra and K. S. Knight, *Phys. Rev. B: Condens. Matter Mater. Phys.*, 1995, **52**, 12790–12797.

22 I. Felner and I. Nowik, *Phys. Rev. B: Condens. Matter Mater. Phys.*, 1986, **33**, 617–619.

23 I. Felner, I. Nowik, D. Vaknin, U. Potzel, J. Moser, G. M. Kalvius, G. Wortmann, G. Schmiester, G. Hilscher, E. Gratz, C. Schmitzer, N. Pillmayr, K. G. Prasad, H. de Waard and H. Pinto, *Phys. Rev. B: Condens. Matter Mater. Phys.*, 1987, **35**, 6956–6963.

24 H. Müller, E. Bauer, E. Gratz, K. Yoshimura, T. Nitta and M. Mekata, *J. Magn. Magn. Mater.*, 1988, **76**, 159–160.

25 E. V. Sampathkumaran, L. C. Gupta, R. Vijayaraghavan, K. V. Gopalakrishnan, R. G. Pillay and H. G. Devare, *J. Phys. C: Solid State Phys.*, 1981, **14**, L237.

26 M. Croft, J. A. Hodges, E. Kemly, A. Krishnan, V. Murgai and L. C. Gupta, *Phys. Rev. Lett.*, 1982, **48**, 826–829.

27 L. Fournes, B. Chevalier, B. Lloret and J. Etourneau, *Z. Phys. B: Condens. Matter*, 1989, **75**, 501–505.

28 C. U. Segre, M. Croft, J. A. Hodges, V. Murgai, L. C. Gupta and R. D. Parks, *Phys. Rev. Lett.*, 1982, **49**, 1947–1950.

29 M. Radzieowski, F. Stegemann, T. Block, J. Stahl, D. Johrendt and O. Janka, *J. Am. Chem. Soc.*, 2018, **140**, 8950–8957.

30 F. Stegemann, J. Stahl, M. Bartsch, H. Zacharias, D. Johrendt and O. Janka, *Chem. Sci.*, 2019, **10**, 11086–11094.

31 O. Janka, O. Niehaus, R. Pöttgen and B. Chevalier, *Z. Naturforsch.*, 2016, **71b**, 737–764.

32 R. Pöttgen and B. Chevalier, *Z. Naturforsch.*, 2015, **70b**, 289–304.

33 R. Pöttgen and B. Chevalier, *Z. Naturforsch.*, 2015, **70b**, 695–704.

34 R. Pöttgen, O. Janka and B. Chevalier, *Z. Naturforsch.*, 2016, **71b**, 165–191.

35 S. F. Matar, *Prog. Solid State Chem.*, 2013, **41**, 55–85.

36 S. Gupta and K. G. Suresh, *J. Alloys Compd.*, 2015, **618**, 562–606.

37 S. Engel, E. C. J. Gießelmann, R. Pöttgen and O. Janka, *Rev. Inorg. Chem.*, 2023, **43**, 571–582.

38 S. Engel, E. C. J. Gießelmann, M. K. Reimann, R. Pöttgen and O. Janka, *ACS Org. Inorg. Au*, 2024, **4**, 188–222.

39 S. Engel, J. Bönnighausen, F. Stegemann, R. S. Touzani and O. Janka, *Z. Naturforsch.*, 2022, **77**, 367–379.

40 A. I. Tursina, N. G. Bukhan'ko, A. V. Gribanov, V. A. Shchelkunov and Y. V. Nelyubina, *Acta Crystallogr., Sect. E: Struct. Rep. Online*, 2005, **E61**, i285–i286.

41 T. Koizumi, F. Honda, Y. J. Sato, D. Li, D. Aoki, Y. Haga, J. Gouchi, S. Nagasaki, Y. Uwatoko, Y. Kaneko and Y. Ōnuki, *J. Phys. Soc. Jpn.*, 2022, **91**, 043704.

42 R. Pöttgen, T. Gulden and A. Simon, *GIT Labor-Fachz.*, 1999, **43**, 133–136.

43 *Topas, Version 5 Version 5*, Bruker AXS Inc., Karlsruhe (Germany), 2014.

44 J. Bönnighausen, S. Seidel, S. Klenner and R. Pöttgen, *Z. Kristallogr.*, 2021, **236**, 293–300.

45 D. Langen, Dissertation, Universität zu Köln, 1997.

46 G. M. Sheldrick, SADABS University of Göttingen, Germany, 1996.

47 P. J. Becker and P. Coppens, *Acta Crystallogr., Sect. A: Cryst. Phys., Diffr., Theor. Gen. Crystallogr.*, 1974, **30**, 129–147.

48 *Topspin Version 2.1*, Bruker Corp., Karlsruhe, 2008.

49 D. Massiot, F. Fayon, M. Capron, I. King, S. Le Calvé, B. Alonso, J.-O. Durand, B. Bujoli, Z. Gan and G. Hoatson, *Magn. Reson. Chem.*, 2002, **40**, 70–76.

50 P. E. Blöchl, *Phys. Rev. B: Condens. Matter Mater. Phys.*, 1994, **50**, 17953–17979.

51 G. Kresse and D. Joubert, *Phys. Rev. B: Condens. Matter Mater. Phys.*, 1999, **59**, 1758–1775.

52 G. Kresse and J. Furthmüller, *Phys. Rev. B: Condens. Matter Mater. Phys.*, 1996, **54**, 11169–11186.

53 G. Kresse and J. Furthmüller, *Comput. Mater. Sci.*, 1996, **6**, 15–50.

54 J. P. Perdew, K. Burke and M. Ernzerhof, *Phys. Rev. Lett.*, 1996, **77**, 3865–3868.

55 E. Sanville, S. D. Kenny, R. Smith and G. Henkelman, *J. Comput. Chem.*, 2007, **28**, 899–908.

56 G. Henkelman, A. Arnaldsson and H. Jónsson, *Comput. Mater. Sci.*, 2006, **36**, 354–360.

57 W. Tang, E. Sanville and G. Henkelman, *J. Phys.: Condens. Matter*, 2009, **21**, 084204.

58 O. K. Andersen, R. W. Tank and O. Jepsen, *TB-LMTO-ASA version 4.7*, Max-Planck-Institut für Festkörperforschung, Stuttgart (Germany), 1998.

59 D. D. Koelling and B. N. Harmon, *J. Phys. C: Solid State Phys.*, 1977, **10**, 3107.

60 W. R. L. Lambrecht and O. K. Andersen, *Phys. Rev. B: Condens. Matter Mater. Phys.*, 1986, **34**, 2439–2449.

61 L. G. Akselrud, V. I. Yarovets, O. I. Bodak, Y. P. Yarmolyuk and E. I. Gladyshevskii, *Kristallografiya*, 1976, **21**, 383–386.

62 A. I. Tursina, E. V. Murashova, H. Noël, N. G. Bukhan'ko and Y. D. Seropegin, *Intermetallics*, 2009, **17**, 780–783.

63 J. Comer, *Acta Crystallogr.*, 1964, **17**, 444–445.

64 M. Ellner, U. Kattner and B. Predel, *J. Less-Common Met.*, 1982, **87**, 305–325.

65 L. Palatinus and G. Chapuis, *J. Appl. Crystallogr.*, 2007, **40**, 786–790.

66 V. Petříček, M. Dušek and L. Palatinus, *Jana2006. The crystallographic computing system Institute of Physics*, Praha (Czech Republic), 2006.

67 V. Petříček, M. Dušek and L. Palatinus, *Z. Kristallogr.*, 2014, **229**, 345–352.

68 P. Villars and K. Cenzual, *Pearson's Crystal Data: Crystal Structure Database for Inorganic Compounds release 2023/24*, ASM International®, Materials Park, Ohio, USA, 2023.

69 N. Zaremba, M. Krnel, Y. Prots, M. König, L. Akselrud, Y. Grin and E. Svanidze, *Inorg. Chem.*, 2024, **63**, 4566–4573.

70 V. B. Compton and B. T. Matthias, *Acta Crystallogr.*, 1959, **12**, 651–654.

71 T. M. Gumenyuk, Y. B. Kuz'ma and B. M. Stel'makhovych, *J. Alloys Compd.*, 2000, **299**, 213–216.

72 B. Erdmann and C. Keller, *J. Solid State Chem.*, 1973, **7**, 40–48.

73 J. Emsley, *The Elements*, Clarendon Press, Oxford University Press, Oxford, New York, 1998.

74 A. E. Dwight, *J. Less-Common Met.*, 1984, **102**, L9–L13.

75 M. Radziewowski, F. Stegemann, C. Doerenkamp, S. F. Matar, H. Eckert, C. Dosche, G. Wittstock and O. Janka, *Inorg. Chem.*, 2019, **58**, 7010–7025.

76 V. M. T. Thiede, B. Fehrmann and W. Jeitschko, *Z. Anorg. Allg. Chem.*, 1999, **625**, 1417–1425.

77 F. Eustermann, S. Gausebeck, C. Dosche, M. Haensch, G. Wittstock and O. Janka, *Crystals*, 2018, **8**, 169.

78 C. Benndorf, F. Stegemann, H. Eckert and O. Janka, *Z. Naturforsch.*, 2015, **70b**, 101–110.

79 S. Engelbert and O. Janka, *Intermetallics*, 2018, **96**, 84–89.

80 C. Benndorf, H. Eckert and O. Janka, *Dalton Trans.*, 2017, **46**, 1083–1092.

81 K. Schubert, W. Burkhardt, P. Esslinger, E. Günzel, H. G. Meissner, W. Schütt, J. Wegst and M. Wilkens, *Naturwissenschaften*, 1956, **43**, 248–249.

82 K. Schubert, H. Breimer, W. Burkhardt, E. Günzel, R. Haufler, H. L. Lukas, H. Vetter, J. Wegst and M. Wilkens, *Naturwissenschaften*, 1957, **44**, 229–230.

83 E. Zintl, A. Harder and W. Haucke, *Z. Phys. Chem., Abt. B*, 1937, **35**, 354–362.

84 A. W. Hull, *Phys. Rev.*, 1917, **10**, 661–696.

85 A. W. Hull, *Trans. Am. Inst. Electr. Eng.*, 1919, **38**, 1445–1466.

86 E. O. Wollan and W. C. Koehler, *Phys. Rev.*, 1955, **100**, 545–563.

87 M. Giovannini, H. Michor, E. Bauer, G. Hilscher, P. Rogl and R. Ferro, *J. Alloys Compd.*, 1998, **280**, 26–38.

88 I. R. Fisher, Z. Islam and P. C. Canfield, *J. Magn. Magn. Mater.*, 1999, **202**, 1–10.

89 Y. Tyvanchuk, S. Baran, T. Jaworska-Gołąb, R. Duraj, Y. M. Kalychak and A. Szytuła, *Acta Phys. Pol., A*, 2012, **121**, 678–681.

90 C. Benndorf, H. Eckert and O. Janka, *Acc. Chem. Res.*, 2017, **50**, 1459–1467.

91 C. Benndorf, O. Niehaus, H. Eckert and O. Janka, *Z. Anorg. Allg. Chem.*, 2015, **641**, 168–175.

92 S. Engel, E. C. J. Gießelmann, L. E. Schank, G. Heymann, K. Brix, R. Kautenburger, H. P. Beck and O. Janka, *Inorg. Chem.*, 2023, **62**, 4260–4271.

93 E. C. J. Gießelmann, S. Engel, J. Baldauf, J. Kösters, S. F. Matar, G. Kickelbick and O. Janka, *Inorg. Chem.*, 2024, **63**, 8180–8193.

94 F. Stegemann, C. Benndorf, T. Bartsch, R. S. Touzani, M. Bartsch, H. Zacharias, B. P. T. Fokwa, H. Eckert and O. Janka, *Inorg. Chem.*, 2015, **54**, 10785–10793.

95 F. Stegemann, C. Benndorf, Y. Zhang, M. Bartsch, H. Zacharias, B. P. T. Fokwa, H. Eckert and O. Janka, *Inorg. Chem.*, 2017, **56**, 1919–1931.

96 F. Stegemann, C. Benndorf, Y. Zhang, M. Bartsch, H. Zacharias, B. P. T. Fokwa, H. Eckert and O. Janka, *Z. Anorg. Allg. Chem.*, 2017, **643**, 1379–1390.

97 C. Benndorf, F. Stegemann, S. Seidel, L. Schubert, M. Bartsch, H. Zacharias, B. Mausolf, F. Haarmann, H. Eckert, R. Pöttgen and O. Janka, *Chem. – Eur. J.*, 2017, **23**, 4187–4196.

98 J. F. Moulder, W. F. Stickle, P. E. Sobol and K. D. Bomben, *Handbook of X-Ray Photoelectron Spectroscopy*, Physical Electronics, Minnesota, 1995.

99 I. Antonyshyn, O. Sichevych, U. Burkhardt, A. M. Barrios Jiménez, A. Melendez-Sans, Y.-F. Liao, K.-D. Tsuei, D. Kasinathan, D. Takegami and A. Ormeci, *Phys. Chem. Chem. Phys.*, 2023, **25**, 31137–31145.

100 J. Heinrich, R. Busch, F. Müller, S. Grandthyll and S. Hüfner, *Appl. Phys. Lett.*, 2012, **100**, 071909.

101 *NIST X-ray Photoelectron Spectroscopy Database, NIST Standard Reference Database Number 20*, National Institute of Standards and Technology, Gaithersburg MD, 20899, 2000, (retrieved Dec. 17th 2023), DOI: **10.18434/T4T88K**.